Available online at www.sciencedirect.com
ScienceDirect
Trans. Nonferrous Met. Soc. China 35(2025) 1956−1974
Transactions of Nonferrous Metals Society of China
www.tnmsc.cn

Microstructure and mechanical properties of high damping Zn−Al eutectoid alloy reinforced by in-situ formed Al_2O_3 and Al_3Zr particles

Jian-jun ZHANG[1], Dong-mei LU[2], Fu-xing YIN[3], Hui YU[1], Pu-guang JI[1], Yu-fang LI[1], Qing-zhou WANG[1]

1. State Key Laboratory of High Performance Roll Materials and Composite Forming, School of Materials Science and Engineering, Hebei University of Technology, Tianjin 300130, China;
2. School of Science, Hebei University of Technology, Tianjin 300130, China;
3. Institute of New Materials, Guangdong Academy of Sciences, Guangzhou 510651, China

Received 10 September 2023; accepted 17 April 2024

Abstract: Zn−Al eutectoid alloy (ZA22) has ultra-high damping property, but its mechanical properties are still relatively low. In order to simultaneously improve the tensile strength and plasticity, a novel Al matrix composite inoculant containing in-situ formed Al_2O_3 and Al_3Zr particles was designed and used to reinforce the ZA22 alloy. The microstructure of the ZA22 alloy was significantly refined. Fine Al_2O_3 particles were uniformly distributed in the α phase and the lamellar eutectoid structure, whereas Al_3Zr particles were distributed in the α phase and at the α/η interface. Property tests showed that the tensile mechanical properties of the reinforced ZA22 alloys were significantly improved. The maximum tensile strength and elongation reached 355 MPa and 7.62%, which were 1.50 and 1.89 times those of the original ZA22 alloy, respectively. The increase in mechanical properties is attributed to the multiple strengthening and toughening factors constructed in the refined microstructure.

Key words: ZA22 alloy; Al_2O_3; Al_3Zr; microstructure refinement; tensile strength; elongation

1 Introduction

In recent years, Zn−Al alloys have been widely used for vibration and noise reduction of electronic devices and instruments due to their high damping capacity and immunity to magnetic fields [1−3]. Especially ZA22 alloy, due to its ultra-high damping capacity and good wear resistance, is expected to be widely used in vibration reduction bearings, oil storage, transportation damping vibrators and other occasions [4−6]. However, although the high damping property of the ZA22 alloy is sufficient to meet the vibration reduction needs of most engineering fields, its relatively low mechanical properties limit its applications in situations with requirement for high load-bearing capacity. Therefore, how to significantly improve the mechanical properties of the ZA22 alloy has become an urgent problem to be resolved.

Many studies have shown that the existence of coarse dendrites of α phase, the composition segregation and the intrinsic low strength of constituent phases are the fundamental reasons for the low mechanical properties of Zn−Al alloys [7−9]. Adding effective inoculants to refine the microstructures should be an effective method to solve these problems and significantly improve the comprehensive mechanical properties [10,11]. YOUSEFI et al [10] refined the microstructures of the ZA22−xSi (x=4 and 8 wt.%) alloy by adding the Ti−B inoculant. They found that the coarse dendrites of α phase were eliminated from the Ti−B treated ZA22−xSi alloys and that the microstructure

Corresponding author: Qing-zhou WANG, Tel: +86-13821156527, E-mail: qzwang@hebut.edu.cn
https://doi.org/10.1016/S1003-6326(25)66793-8

was significantly refined, which also resulted in a more uniform distribution of the phases in the alloys. The tensile strength and fracture strain of the refined ZA22−4Si and ZA22−8Si alloys were significantly improved. SKENAZI et al [11] reported that the introduction of AlB_3, $AlTi_5B_1$ and $AlZr_5$ inoculants into Zn−Al alloys could refine the microstructures and improve the tensile strength and elongation.

Although the above studies have achieved the goal of improving the mechanical properties through microstructure refinement, the degree of property improvement is still limited due to the single strengthening mechanism. Recently, it has been found that the combined addition of inoculant and trace amount of Ce or Zr elements to ZA22 alloy was superior to the individual addition of Al−5Ti−B inoculant in terms of overall property improvement, which was related to the introduction of a dual strengthening mechanism [4,5]. In addition, in our previous work [12], (Al_3Ni+Al_3Ti)/Al composite inoculant was fabricated and used to refine the ZA22 alloy. It was found that due to the fine grain strengthening effect caused by Al_3Ti particles, as well as the dispersion strengthening effect caused by Al_3Ni particles, the mechanical properties of the refined ZA22 alloy were significantly improved, and its improvement effect is better than that relying solely on fine grain strengthening [12]. Therefore, composite inoculant can introduce other strengthening effects, rather than just fine grain strengthening effect, thus resulting in better mechanical properties.

Ceramic particles are one of the important reinforcing materials for metal matrix composites (MMCs) [13−15]. Many researchers found that the uniform dispersion of ceramic oxides (ZrO_2/Al_2O_3), nitrides (TiN/Si_3N_4) and carbides (SiC/TiC) in Al alloys could significantly improve the mechanical properties [16−19]. Special attention should be paid to Al_2O_3 particles. Al_2O_3 particles have very high strength and hardness, excellent wear resistance, high-temperature stability, and chemical stability, making them the most promising and irreplaceable reinforcing material in Al matrix composites (AMCs) [20−22]. In this study, a novel AMC inoculant containing Al_2O_3 and Al_3Zr particles was designed and used to significantly improve the mechanical properties of the ZA22 alloy through the fine grain strengthening effect of inoculant and the dispersion strengthening effect of Al_2O_3. It is expected that this study can provide an important theoretical basis for the design and fabrication of high-efficiency composite inoculant for Zn and Al matrix alloys and the development of novel high-strength and high-damping alloys.

2 Experimental

2.1 Fabrication of (Al_2O_3+Al_3Zr)/Al composite inoculant and its inoculated ZA22 alloy

(Al_2O_3+Al_3Zr)/Al composite inoculant was fabricated by melting pure aluminum (purity > 99.9%) and commercial $Zr(CO_3)_2$ powders in a vacuum electric arc furnace (three mass ratios of Al/$Zr(CO_3)_2$ were used: 95:5, 85:15 and 75:25). To guarantee the uniformity of compositions, the obtained buttons were repeatedly melted at least five times. The ZA22 alloy was fabricated in an electric resistance furnace by using high-purity Zn and Al metals (purity > 99.9%) as raw materials. When the ZA22 alloy was melted at 650 °C (The melting point and eutectoid transformation temperature of ZA22 alloy were 430 and 275 °C, respectively [5]), composite inoculant with different contents (0.7, 0.8, 0.9, 1.0 and 1.1 wt.%) was added to the melt. After stirring for 5 min, the melt was poured into a cylindrical steel mold.

2.2 Structure characterization

Optical microscope (OM, BX41M Olympus) and field emission scanning electron microscope (FESEM, Quanta 450 FEG) equipped with an energy dispersive spectrometer (EDS) were used to observe the microstructures of specimens, and electron probe microanalysis (EPMA, JEOL 8530F) was used to get the elemental distribution maps. Before microscopic observation, the specimens were ground with $240^{\#}$−$2000^{\#}$ grit SiC sand papers, then polished with diamond paste until they had mirror-like surface, and finally etched by the solution of 0.5 vol.% HF. The size of α phase in the ZA22 alloy was measured by the linear intercept method through the SISC IAS V8.0 image software. The phase composition was identified by X-ray diffraction (XRD, Bruker D8 Discover) with Cu K_α radiation. Transmission electron microscope (TEM, TecnaiG2−F30) was used to further observe the microstructures and interfaces. TEM specimens with a thickness of 1.0 mm were first mechanically

ground to around 60 μm, then punched to *d*3 mm circle sheets, and finally thinned by ion milling to get the electron transparent area to fit for conventional bright field and dark field (BF and DF) as well as HRTEM imaging. Differential scanning calorimetry (DSC, TA-Q20) was used to track the phase transition of different ZA22 alloys during heating and cooling processes from 150 to 500 °C. The temperature changing rate was 10 °C/min. The specimen had a mass of 8 mg and was placed in a nitrogen atmosphere during the experiment. The electron backscattered diffraction (EBSD, JSM−7200F) was used to characterize the grains, grain boundary and phase distribution of the specimens, and the specimens were processed by ion beam polishing technique.

2.3 Property tests

Tensile mechanical property tests were performed on the universal testing machine (UTM, INSTRON) with a deformation rate of 2 mm/min at room temperature. The tensile specimens with a gauge length of 25 mm and a cross-section of *d*5 mm were machined according to the GB/T228.1—2010 (ISO 6892:1998) standard. At least three specimens were measured for each alloy to ensure the repeatability of the results. Internal friction (IF), Q^{-1}, was used to characterize the damping property, and it was measured on a dynamic mechanical analyzer (DMA, Q800) in the temperature range from room temperature to 400 °C with a heating rate of 5 °C/min. The size of the internal friction specimens was 35 mm × 10 mm × 2 mm.

3 Results and discussion

3.1 Characteristics of (Al_2O_3+Al_3Zr)/Al composite inoculant and ZA22 alloy

Figure 1 shows the XRD patterns of the (Al_2O_3+Al_3Zr)/Al composite inoculant. It can be seen that the inoculant is mainly composed of Al matrix, Al_2O_3 and Al_3Zr phases. With the increase of the content of $Zr(CO_3)_2$, both the intensity and the number of diffraction peaks of Al_2O_3 and Al_3Zr phases increase. The reactions that occur during the melting process of the inoculant can be expressed as follows [23−25]:

$$Zr(CO_3)_2=ZrO_2+2CO_2(g) \quad (1)$$

$$3ZrO_2+4Al=3[Zr]+2Al_2O_3 \quad (2)$$

$$[Zr]+3Al=Al_3Zr \quad (3)$$

As shown in Reaction (1), during the melting process of the inoculant in a vacuum arc furnace, $Zr(CO_3)_2$ powder will decompose into ZrO_2 and CO_2. The product ZrO_2 will next participate in the reaction as shown in Reaction (2). According to the results reported in Ref. [25], the variation of the standard Gibbs free energy change (ΔG_T^{Θ}) of Reaction (2) can be expressed by $\Delta G_T^{\Theta}=-176603+54.63T$ (T is the thermodynamic temperature). Let $\Delta G_T^{\Theta}=0$, then T=2960 °C. In this study, the melting process was carried out at temperatures below 2960 °C, indicating that Reaction (2) can occur spontaneously. The standard Gibbs free energy change of Al_2O_3 is much lower than that of Al_3Zr, making the fact that the formation priority and stability of the Al_2O_3 phase will be much higher than those of the Al_3Zr phase [25]. According to the Al−Zr phase diagram [26], at temperatures above 800 °C, Zr and Al will combine to form Al_3Zr, as shown in Reaction (3). The products of the above three reactions are consistent with the results shown in Fig. 1.

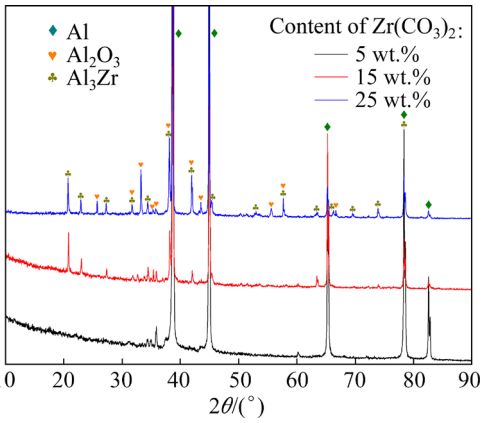

Fig. 1 XRD patterns of (Al_2O_3+Al_3Zr)/Al composite inoculant

Figures 2(a) and (b) show the EPMA maps of the (Al_2O_3+Al_3Zr)/Al composite inoculant in two different regions. From Fig. 2(a), it can be seen that in addition to the gray Al matrix, there are also a large number of white and dark gray phases. According to the elemental maps, it can be identified that the white phase is Al_3Zr, and the dark gray phase is Al_2O_3. In addition, it can also be found that the Al_3Zr phase has striped, blocky, and granular shapes, whereas the Al_2O_3 phase only has granular shape. Figure 2(b) shows a region where Al_3Zr and Al_2O_3 phases have relatively uniform sizes. Interestingly, as shown in Figs. 2(c) and (d), a

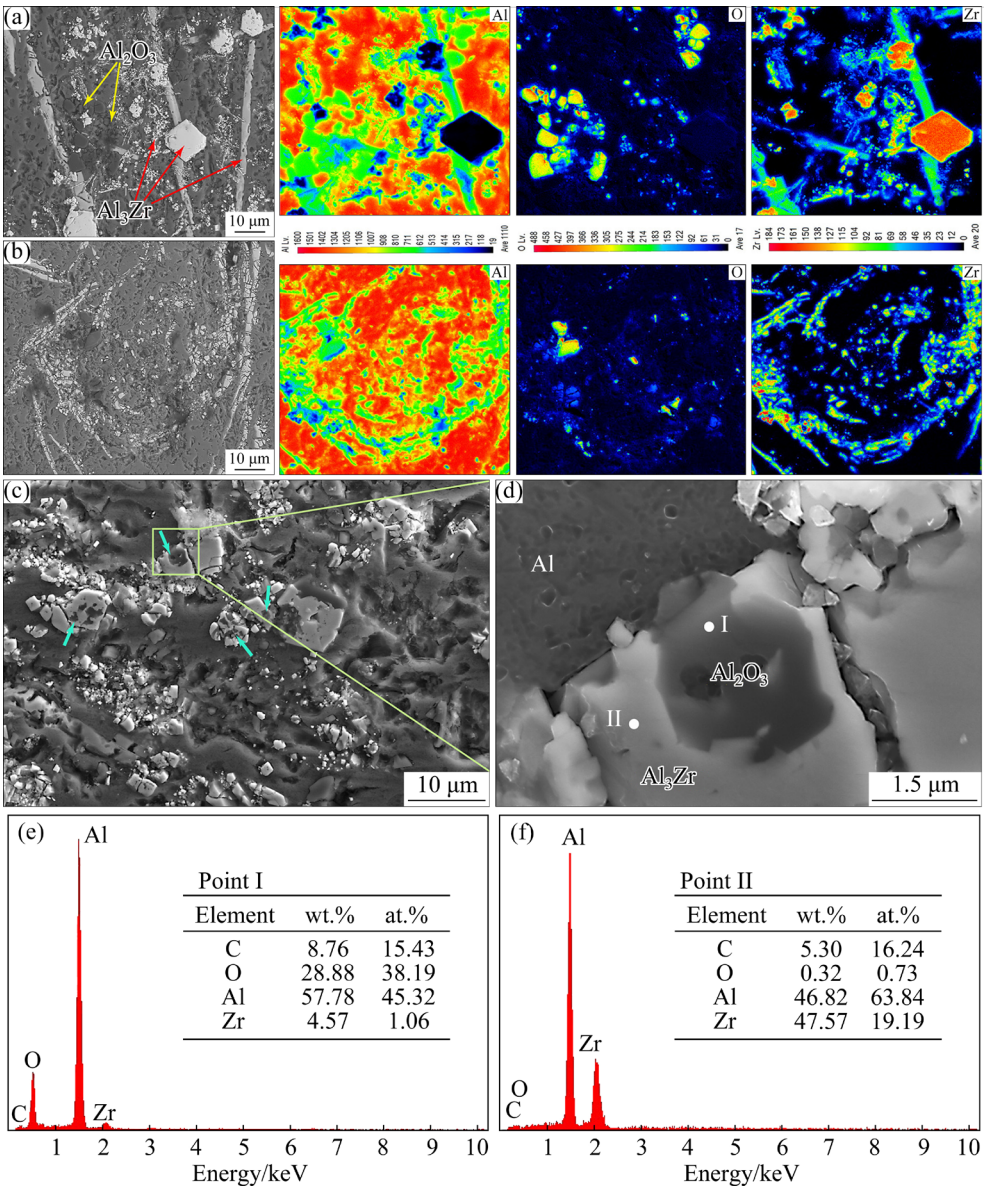

Fig. 2 (a, b) EPMA maps of (Al_2O_3+Al_3Zr)/Al composite inoculant in two different regions; (c) SEM image showing Al_2O_3, Al_3Zr and A_2O_3/Al_3Zr particles; (d) Image with high magnification of region marked by box in (c); (e, f) EDS results of Points I and II marked in (d), respectively

special Al_2O_3/Al_3Zr composite structure is formed in the inoculant. In this special structure, Al_2O_3 particle is embedded inside the Al_3Zr particle.

Figure 3 shows the micrographs of the ZA22 alloy refined by different contents of inoculant. It can be seen that the (Al_2O_3+Al_3Zr)/Al composite inoculant has a significant refining effect on the ZA22 alloy. When 1.0 wt.% inoculant is added, the best refining effect can be achieved, and the α phase is refined to 14 μm. Furthermore, with the increase of the content of inoculant, the morphology of the α phase undergoes an evolution process as shown in Fig. 4.

Figure 5 shows the EPMA maps of the ZA22 alloy refined by 1.0 wt.% inoculant. From Fig. 5(a), it can be seen that a large number of white particles are uniformly distributed in the ZA22 alloy matrix after inoculation. These particles are almost entirely located at the center of the nearly equiaxed α phase. According to Fig. 5(c), these particles can be identified as Al_2O_3 and Al_3Zr. The image of Al_2O_3 particles with a high magnification is shown in Fig. 5(d). It can be seen that Al_2O_3 particle with a size of about 2 μm is covered by a thin film of α phase, indicating that the Al_2O_3 particle is also located at the center of α phase in the 3D space.

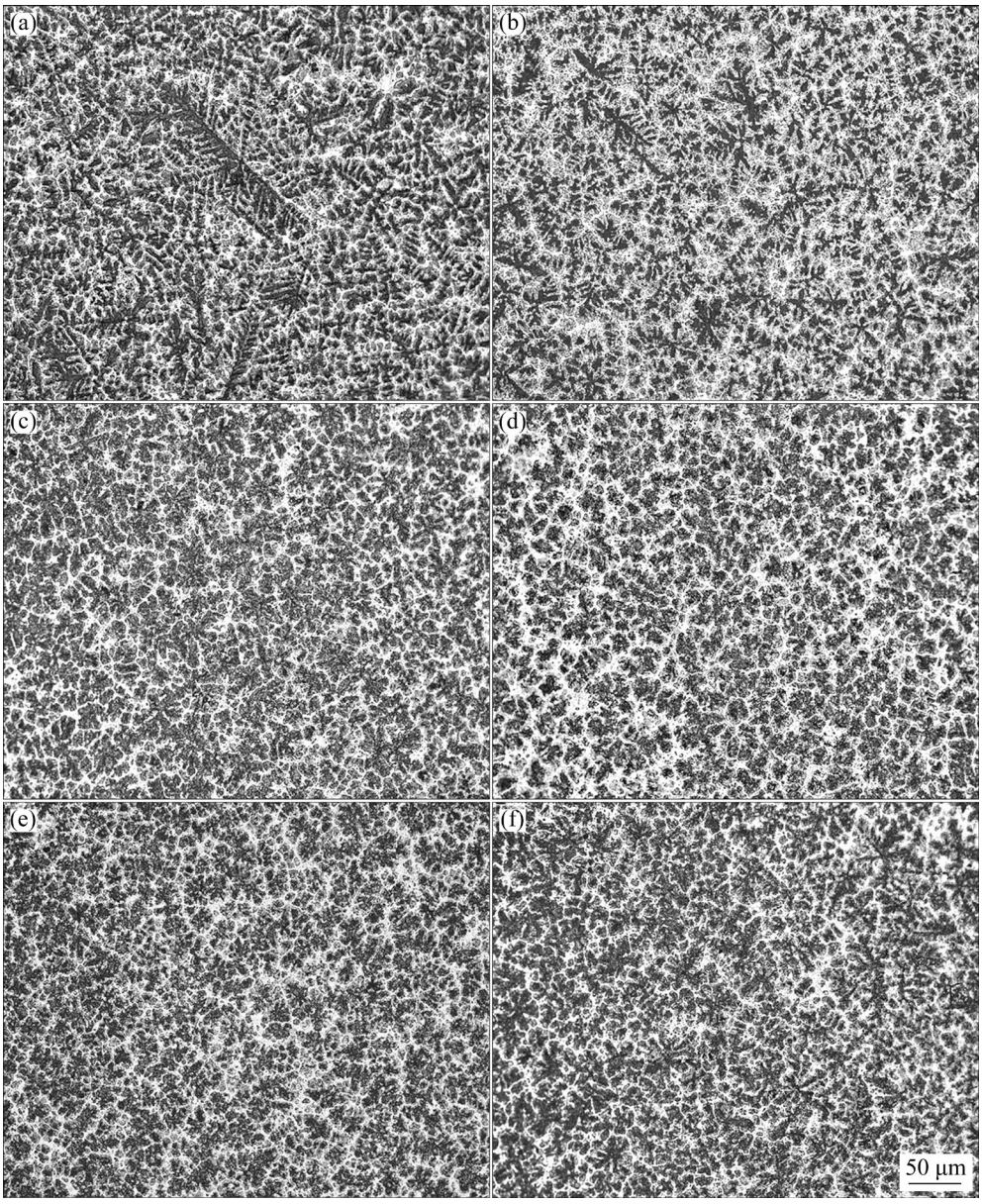

Fig. 3 Optical metallographic microstructures of ZA22 alloy inoculated by different contents of inoculant: (a) 0; (b) 0.7 wt.%; (c) 0.8 wt.%; (d) 0.9 wt.%; (e) 1.0 wt.%; (f) 1.1 wt.%

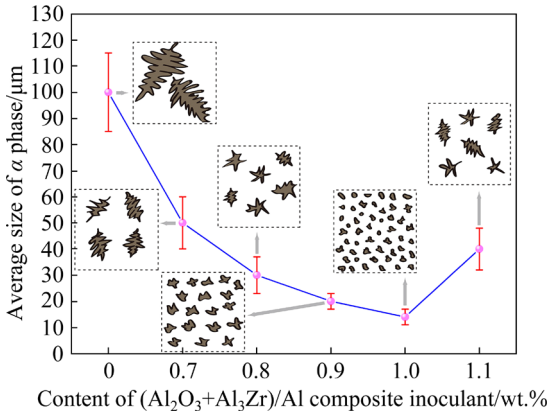

Fig. 4 Effect of (Al_2O_3+Al_3Zr)/Al composite inoculant content on average size and morphology of α phase in ZA22 alloy

From Fig. 5(e), a composite structure is found at the center of α phase. According to the EPMA analysis result, it can be confirmed that the white phase at the bottom is Al_2O_3, and the black phase at the top is Al_3Zr. Obviously, this Al_2O_3/Al_3Zr composite structure is just the composite structure found in Fig. 2(c). In addition to the Al_2O_3 and Al_3Zr particles with a particle size of about 2 μm, a large number of sub-micron sized particles can also be found in Fig. 5(b). They are uniformly distributed in fine lamellar eutectoid structure. Combined with the EPMA analysis results shown in Fig. 5(f), these particles can be identified as Al_2O_3.

Figures 5(g−i) show the SEM images of Al_2O_3

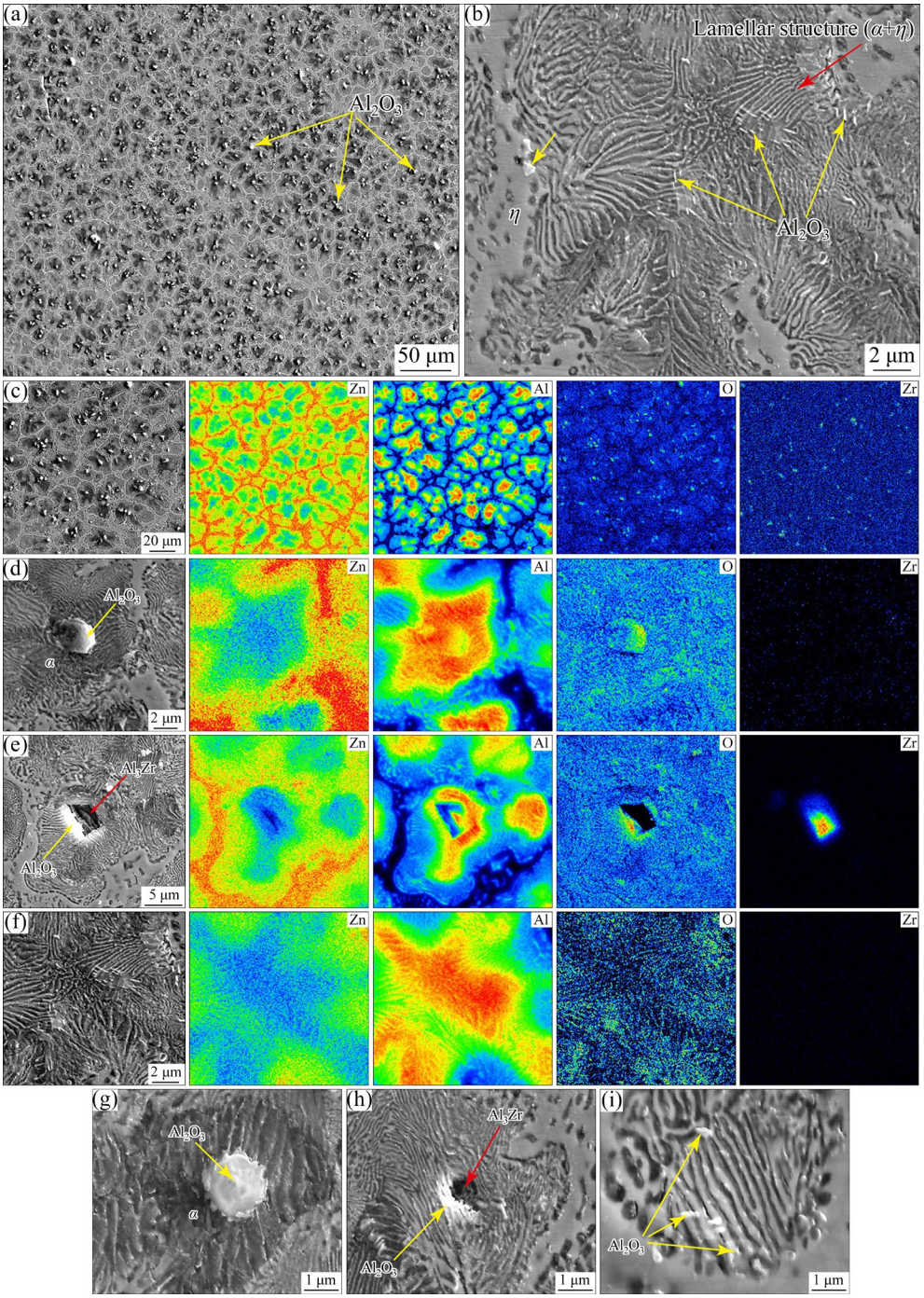

Fig. 5 (a, b) Microstructures in refined ZA22 alloy; (c) EPMA maps of region selected from (a); (d−f) EPMA maps of Al_2O_3 particles, Al_3Zr/Al_2O_3 composite structure and lamellar eutectoid structure; (g−i) SEM images of Al_2O_3 particles, Al_3Zr/Al_2O_3 composite structure and lamellar eutectoid structure in another region

particles, Al_3Zr/Al_2O_3 composite structure and lamellar eutectoid structure in another region. From the figures, it can be seen that the structures are similar to those shown in Figs. 5(c−e). In addition to the locations of Al_2O_3 and Al_3Zr particles mentioned above, from Fig. 6 it can be seen that some Al_3Zr particles are also located at the α/η interface. It is worth noting that the size of the particles in Figs. 5(d, e, g, h) is about 2 μm, but it is clear that there are also much larger Al_2O_3 particles (5−7 μm) located in the α phase shown in Figs. 5(a) and (c). Therefore, the following conclusions can be drawn: Al_2O_3 particles with a size of 2−7 μm are located at the α phase, whereas the Al_2O_3 particles with a size of less than 1 μm are embedded in the lamellar eutectoid structure or adjacent to the η

phase. Some Al_3Zr particles with a size of about 2 μm are located at the α phase, whereas others are located at the α/η interface.

To characterize the morphology and size of grains as well as the grain boundary characteristics, EBSD technology was used, and the results are shown in Figs. 7−10. From Fig. 7, it can be seen that the morphology and grain size of the α phase in

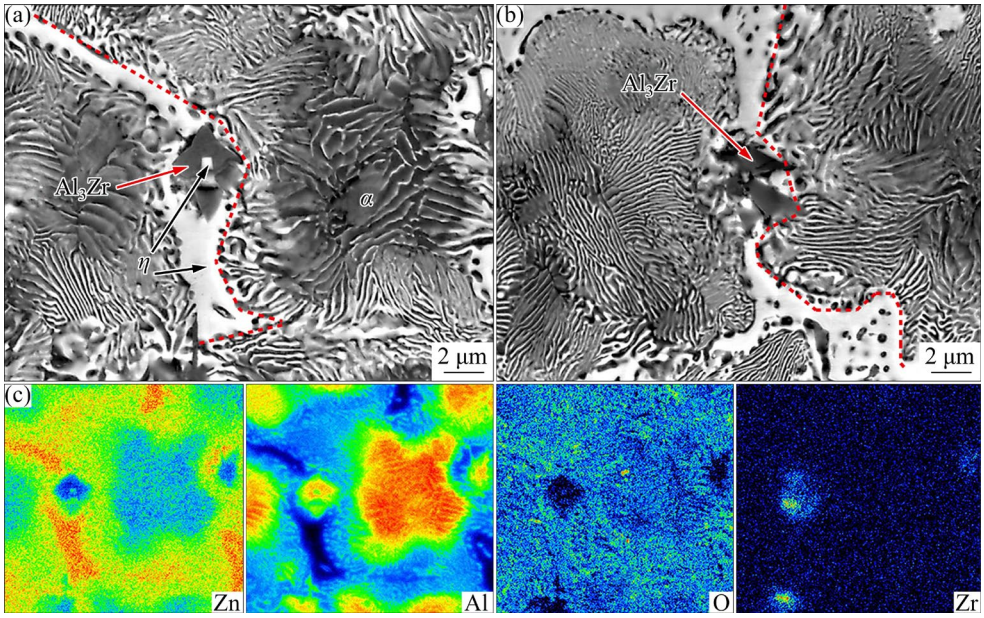

Fig. 6 (a, b) SEM images of Al_3Zr particles located at α/η interface; (c) EPMA maps of (a)

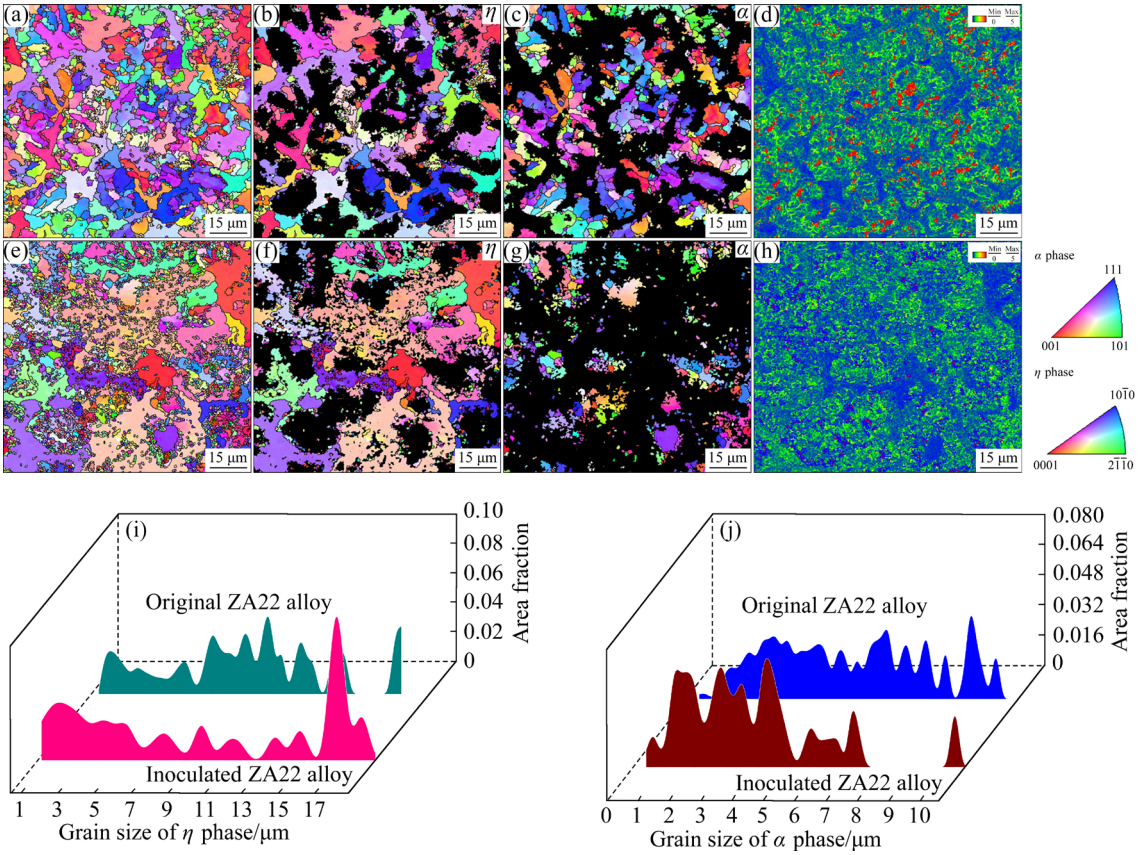

Fig. 7 (a, e) IPF maps of original and inoculated ZA22 alloys; (b, c) IPF maps of η and α phases in (a), respectively; (f, g) IPF maps of η and α phases in (e), respectively; (d, h) KAM maps corresponding to (a) and (e), respectively; (i, j) Grain size distribution of η and α phases in original and inoculated ZA22 alloys, respectively

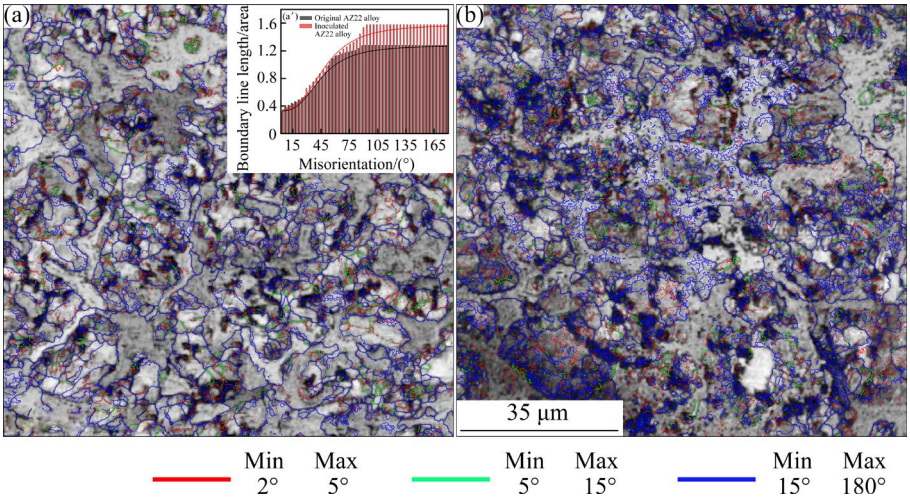

Fig. 8 Grain boundary distribution of original (a) and inoculated (b) ZA22 alloys with their grain boundary density (a′)

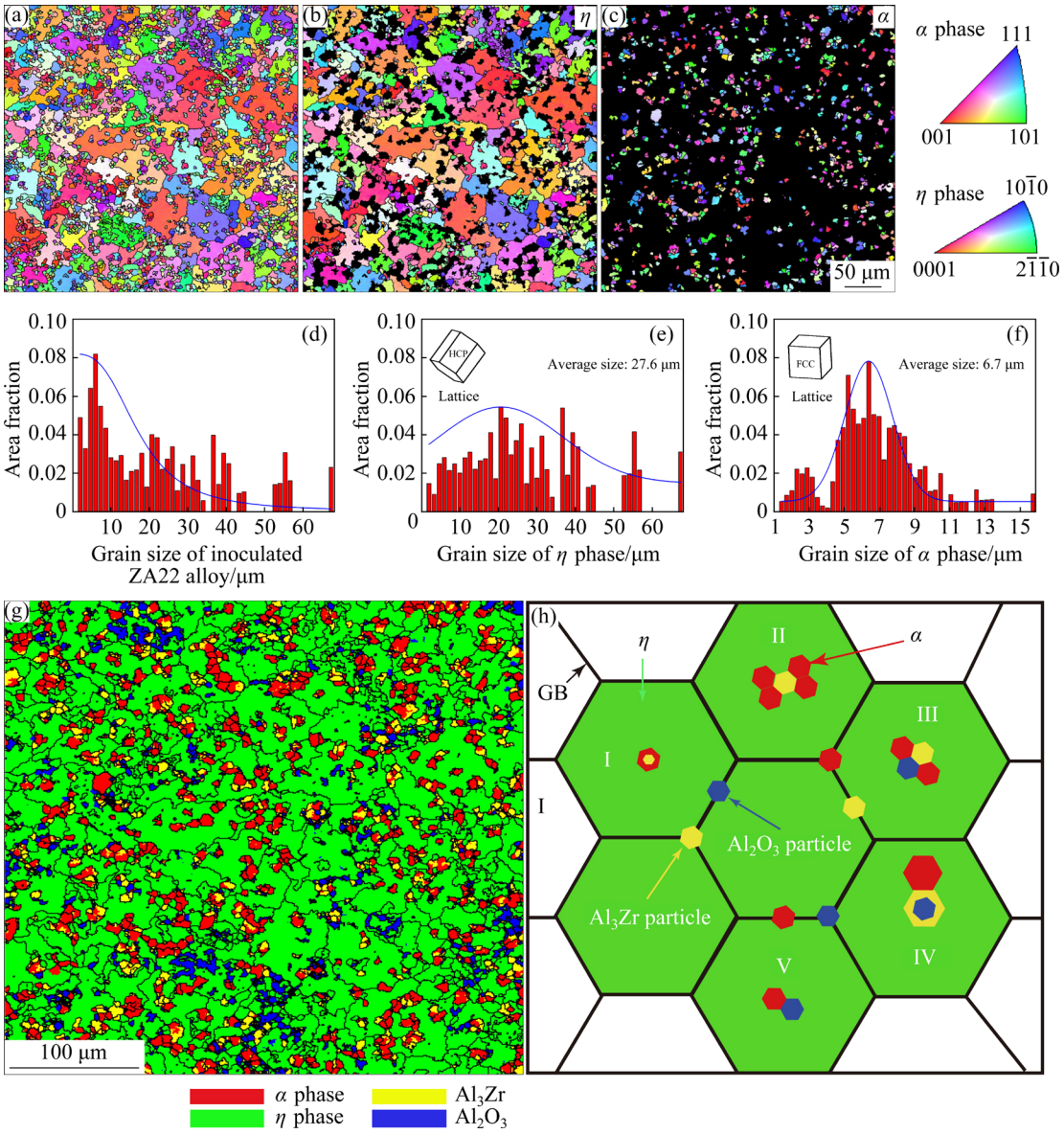

Fig. 9 (a) IPF map of inoculated ZA22 alloy; (b, c) IPF maps of η and α phases in (a), respectively; (d−f) Grain size distribution; (g) Phase distribution; (h) Schematic diagram of phase distribution characteristics

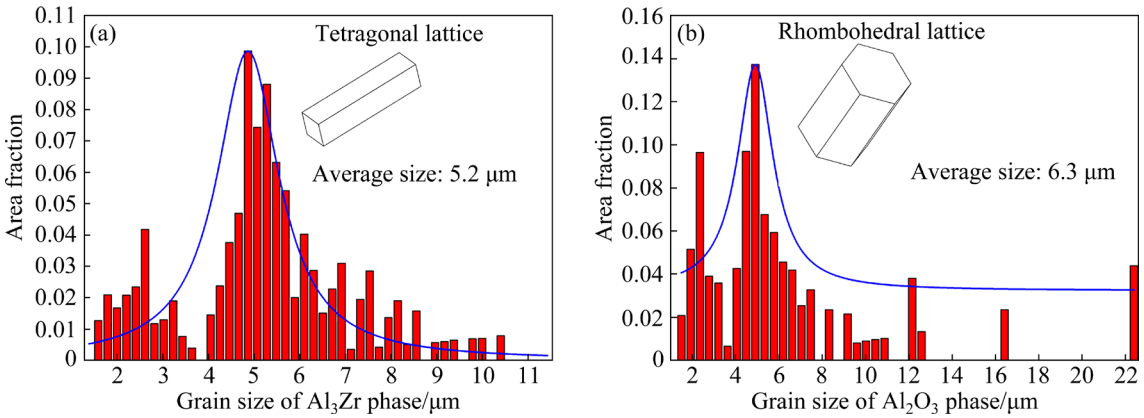

Fig. 10 Grain size distribution of Al_3Zr (a) and Al_2O_3 (b) particles in inoculated ZA22 alloy

the ZA22 alloy are obviously different before and after inoculation. The morphology of the α phase undergoes a transition from rod-shaped to nearly equiaxed shape, and the grain size is refined to 1−5 μm from the original 2−10 μm. Although the grains of the α phase in the size range of 5−10 μm are also present at some locations in the inoculated ZA22 alloy, their content is very low. It is this significant change in the shape and size of the α phase grains that leads to much lower stress concentration in the inoculated ZA22 alloy compared to the original ZA22 alloy, as indicated by the KAM (Kernel average misorientation) maps shown in Figs. 7(d) and (h).

Figures 8(a) and (b) visually display the changes in grain boundary characteristics of the ZA22 alloy before and after inoculation, respectively. It is apparent that the grain boundary density, especially the high angle grain boundary density significantly increases after inoculation. Figure 9 shows the EBSD analysis results of the refined ZA22 alloy at a low magnification. From Figs. 9(a−c), it is found that a dual-phase mixed fine structure is formed in the refined ZA22 alloy, which is composed of η phase with an average grain size of 27.6 μm and α phase with an average grain size of 6.7 μm. The α phase may be distributed inside the η phase or at the boundary of η phase. The grains of both α phase and η phase have lost their sharp features and exhibit a nearly equiaxed shape.

In order to make clear the distribution of Al_2O_3 and Al_3Zr particles in the α phase and η phase, Fig. 9(g) gives the phase distribution diagram. Combined with the schematic diagram shown in Fig. 9(h), it can be concluded as follows: (1) Some Al_2O_3 and Al_3Zr particles are randomly distributed at the grain boundaries of η phase. (2) Some Al_3Zr particles are located inside the grains of α phase, as shown in Fig. 9(h)-I, and some Al_3Zr particles are located at the center of several grains of α phase, as shown in Fig. 9(h)-II. (3) Al_3Zr particle grows along a certain crystal plane of Al_2O_3 particle, and then the grains of α phase grow epitaxially along certain crystal planes of these two particles, as shown in Fig. 9(h)-III. (4) Al_2O_3 particle acts as the nucleation center of Al_3Zr particle, and then grains of α phase grow along a certain crystal plane of this composite structure, as shown in Fig. 9(h)-IV. (5) Some grains of α phase grow along a certain crystal plane of Al_2O_3 particles, as shown in Fig. 9(h)-V. In summary, the distribution of Al_2O_3 and Al_3Zr particles in the ZA22 alloy is diverse, which is different from the traditional view that nucleating particles must be located inside the grains to be refined. From Fig. 10, it is clear that the average sizes of Al_2O_3 and Al_3Zr particles are 5−7 μm, which is close to that (6.7 μm) of the grains of refined α phase.

Figure 11 shows the lamellar eutectoid microstructure of ZA22 alloy before and after inoculation. By comparing Figs. 11(a−c), it can be found that the eutectoid structure of the inoculated ZA22 alloy is significantly refined, resulting in an increase in the interface density. The refinement of the eutectoid structure is understandable: when the α phase is refined, the β phase formed through the peritectic reaction ($L+\alpha\rightarrow\beta$) and the lamellar eutectoid structure formed through the eutectoid reaction ($\beta\rightarrow\alpha+\eta$) will also be refined. From Figs. 11(h−k), it is seen that the α phase and the η phase have a coherent interface, whereas from

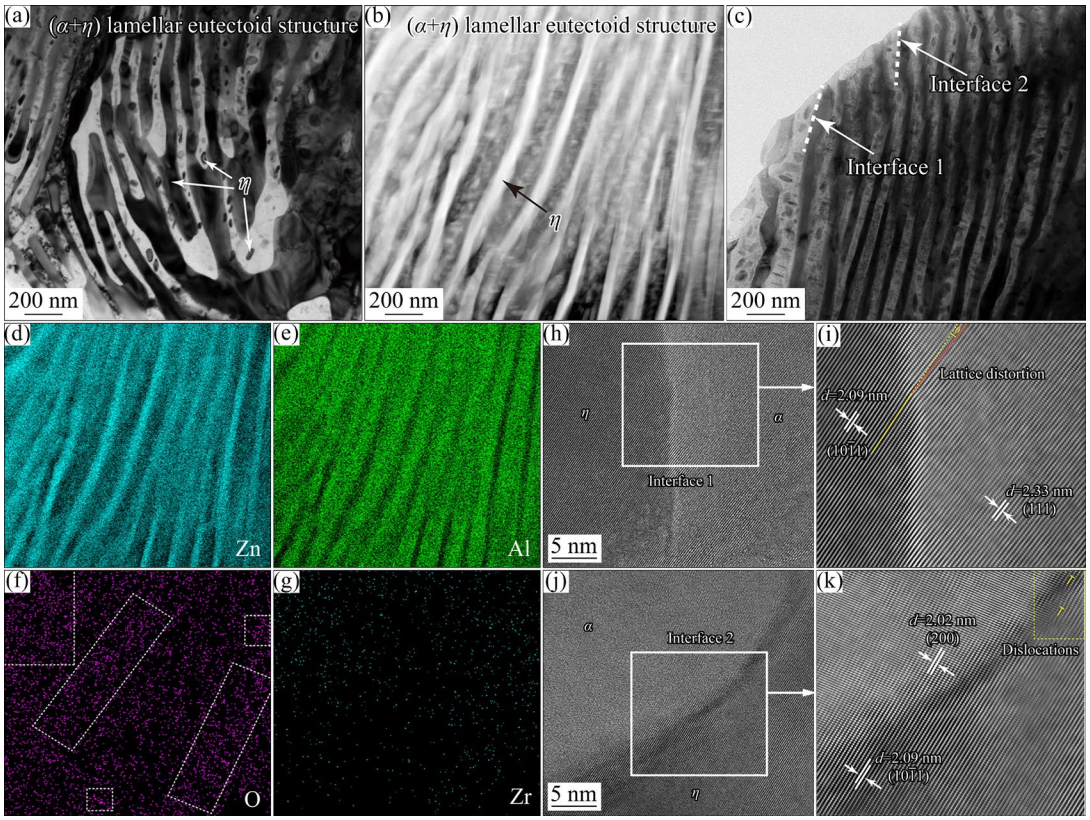

Fig. 11 TEM images of lamellar eutectoid structure in original (a) and inaculated (b, c) ZA22 alloys; (d−g) Elemental maps of (b); (h, j) High resolution images of Interface 1 and 2 marked in (c), respectively; (i, k) IFFT images of selected areas in (h) and (j), respectively

Figs. 11(i) and (k) the lattice distortions and dislocations can be found near the interface due to the differences in lattice spacing between the two phases. This may have a significant impact on the comprehensive properties of the ZA22 alloy, which will be discussed later. It should be noted that according to the EDS analysis results shown in Figs. 11(d−g), the particles in the lamellar eutectoid microstructure should be Al_2O_3, which is in consistency with Fig. 5(b). Since the Al content in the Al_2O_3 particles is much lower than that in the α phase, it is difficult to observe the existence of Al_2O_3 particles in Fig. 11(e). However, in Fig. 11(f), the existence of Al_2O_3 particles can be inferred from the distribution of O element (especially at the locations marked by white dashed boxes).

Figure 12 shows the eutectic structure of the ZA22 alloy before and after inoculation. As shown in Fig. 12(a), there is rod- and strip-shaped white α phase distributed in the black η phase. After inoculation, as shown in Figs. 12(b) and (d), the size of α phase decreases and its shape becomes nearly spherical. From Fig. 12 it can also be found that the density of dislocations decreases after inoculation, indicating that the nearly spherical α phase can reduce the stress concentration in η phase. Figure 12(e) shows the high-resolution image and SAED pattern of the interface between the near-spherical α phase and η phase. It is seen that these two phases have no coherent orientation relationship, which is different from the lamellar eutectoid structure. It is worth noting that a special $\eta@\alpha$ core−shell eutectic structure is found in Figs. 12(b) and (c). As shown in Fig. 12(f), in this special structure, α phase with FCC crystal structure may act as a stress buffer, which plays a positive role in preventing collisions between η phases that may cause microcracking.

The TEM image shown in Fig. 13(a) exhibits a special structure in the inoculated ZA22 alloy: eutectic structure is surrounded by four grains of α phase connected by thin η layer. This special structure has a significant effect on the tensile mechanical properties. SONG et al [27] reported that Zn layers at grain boundary (GB) of α phase contribute to the sliding of GB and rotation of

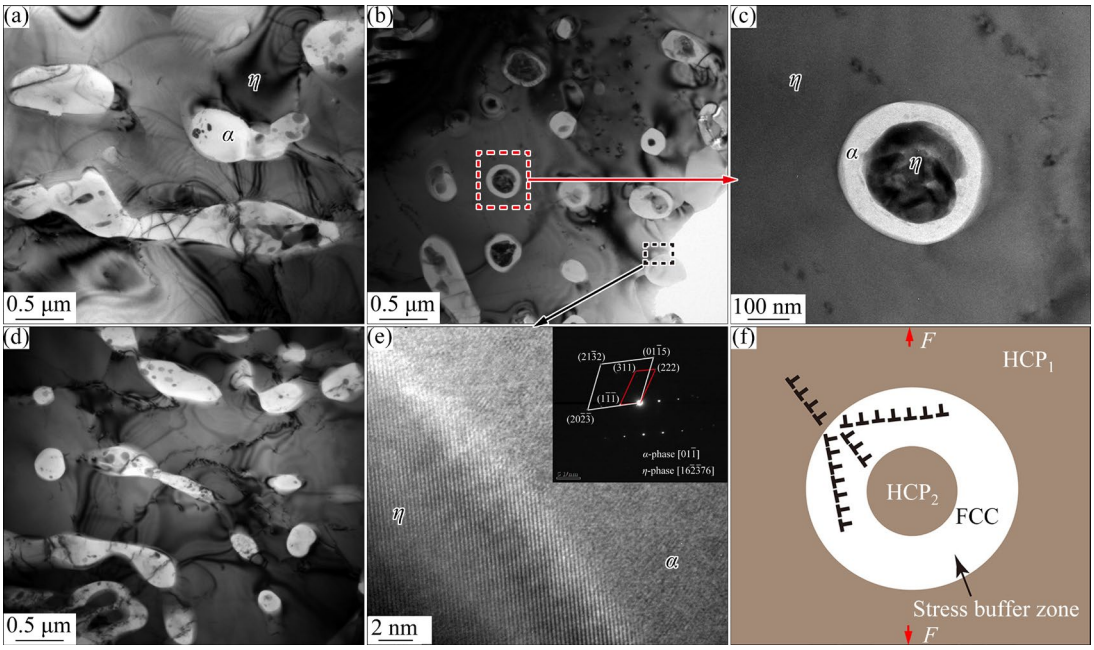

Fig. 12 TEM images of eutectic structure in original (a) and inoculated (b, d) ZA22 alloys; (c) TEM image of area marked with red box in (b); (e) HRTEM images and SAED patterns of area marked with black box in (b); (f) Schematic diagram of dislocation transfer in core−shell eutectic structure under external stresses

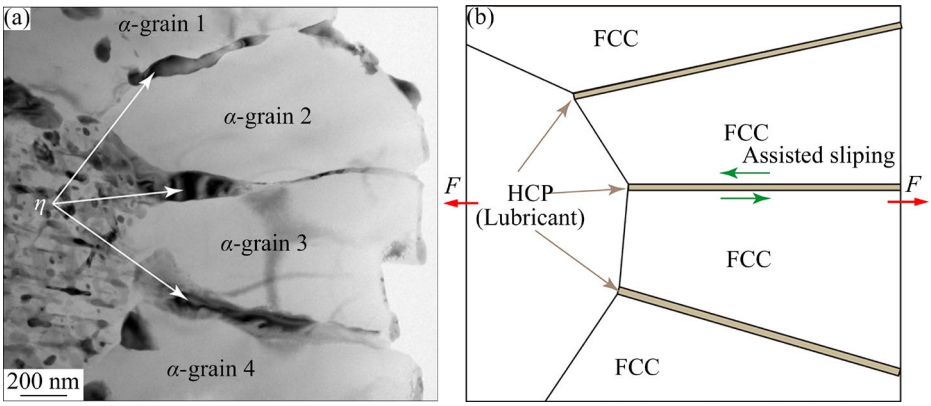

Fig. 13 (a) Special $\alpha/\eta/\alpha$ structure in inoculated ZA22 alloy; (b) Schematic diagram drawn according to structure in (a)

grains at room temperature. Zn layer not only decreases the energy barrier for the sliding of GB, but constructs a two-channel sliding mechanism, which further assists the sliding of GB and the rotation of grains. Grains of Zn phase act as solid lubricants via reorienting the sliding planes of Zn phase. STRAUMAL et al [28] also reported that the presence of Zn thin layer between the Al/Al interfaces was an important reason for excellent plasticity obtained in this alloy. The special structure reported in the above study is consistent with the $\alpha/\eta/\alpha$ structure shown in Fig. 13(a). Thus, as shown in Fig. 13(b), the η phase as a lubricant can assist the sliding of GBs of α grains, leading to the improvement of plasticity of the inoculated ZA22 alloy.

3.2 Effect of Al_3Zr and Al_2O_3 particles on phase transformation behavior of inoculated ZA22 alloy

Figure 14 shows the DSC curves of the original ZA22 alloy and the inoculated ZA22 alloy with the best refining effect. Four exothermic peaks (P1−P4) can be found during cooling process. Combined with the phase diagram of Zn−Al binary alloy [5], these four peaks should correspond to the precipitation of the primary α phase ($L\rightarrow\alpha$), the peritectic reaction ($L+\alpha\rightarrow\beta$), the nonequilibrium

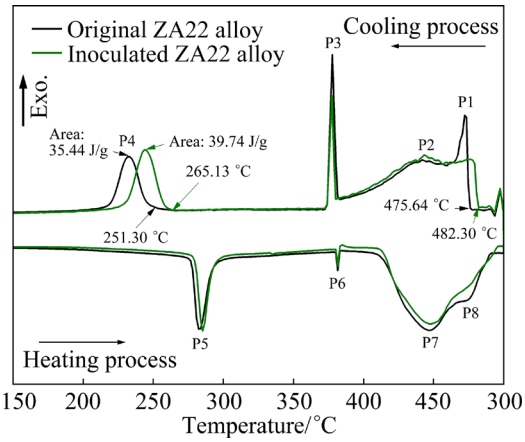

Fig. 14 DSC curves of original and inoculated ZA22 alloys with 1.0 wt.% inoculant

eutectic reaction ($L\rightarrow\beta+\eta$) and the eutectoid transformation ($\beta\rightarrow\alpha+\eta$), respectively. During the heating process, four endothermic peaks (P5−P8) appear, which should correspond to the above four reverse transformation processes of ZA22 alloy [4,5]. Compared with the original ZA22 alloy, the positions of P2 and P3 peaks of the inoculated ZA22 alloy have no change, while the positions of P1 and P4 peaks shift towards the high-temperature side.

The shift of P1 peak can be attributed to the promoting effect of Al_3Zr and Al_2O_3 particles on the nucleation of primary α phase, while the shift of P4 peak can be attributed to the promoting effect of Al_2O_3 particles on the eutectoid transition. In the previous work [12], it was found that the addition of inoculant only affected the position of P1 peak. In this study, a large number of fine Al_2O_3 particles in the inoculant provide nucleation sites for the formation of lamellar eutectoid structure, promoting the occurrence of the eutectoid transformation. In addition, from Fig. 14, it can also be found that the area of P4 peak of the inoculated ZA22 alloy is larger than that of the original ZA22 alloy, which to some extent can reflect the increase in the density of the lamellar eutectoid structure after inoculation.

3.3 Refining mechanism of (Al_2O_3+Al_3Zr)/Al composite inoculant on ZA22 alloy

Whether the Al_2O_3 and Al_3Zr particles in the composite inoculant can play their positive role in refining the ZA22 alloy depends on the interface microstructure and orientation relationships (ORs) between them and the matrix phase of the ZA22 alloy. Figure 15 shows the interfacial microstructure and lattice matching relationship between Al_3Zr phase and α phase. From Figs. 15(b) and (g), it can be seen that the Al_3Zr particle and the α phase have a coherent interface. The OR between them is shown in Figs. 15(e) and (k). According to the figures, the following coherent ORs can be found: $(220)_\alpha//(208)_{Al_3Zr}$, $(111)_\alpha//(114)_{Al_3Zr}$ and $(200)_\alpha//(200)_{Al_3Zr}$. At present, the edge-to-edge matching model (E2EM) is widely used to predict the OR between the secondary phase and the matrix phase [29]. The model is based on the following two criteria [30]:

$$f_p=\frac{|R_B-R_A|}{R_A}\times100\% \tag{4}$$

$$f_a=\frac{|D_B-D_A|}{D_A}\times100\% \tag{5}$$

where f_p is the interplanar spacing misfit of parallel crystal planes, f_a is the interatomic spacing misfit of parallel crystal directions, R_A and R_B are the interplanar spacings of phases A and B, respectively; D_A and D_B are the interatomic spacing of phases A and B, respectively. When f_p<6% and f_a<10%, the interface energy between the two phases will be low enough so that one phase can be used as a nucleation substrate for the other phase. The values of f_p and f_a calculated in this study are shown in the corresponding lattice matching diagrams. Compared with experiments, using this model for prediction is convenient and comprehensive. According to the E2EM model, the possible matching planes between α phase and Al_3Zr phase include $\{111\}_\alpha/\{114\}_{Al_3Zr}$, $\{200\}_\alpha/\{200\}_{Al_3Zr}$, $\{220\}_\alpha/\{220\}_{Al_3Zr}$ and $\{220\}_\alpha/\{208\}_{Al_3Zr}$. The possible matching crystal directions include $\langle110\rangle_\alpha/\langle110\rangle_{Al_3Zr}$, $\langle110\rangle_\alpha/\langle401\rangle_{Al_3Zr}$, $\langle100\rangle_\alpha/\langle100\rangle_{Al_3Zr}$, $\langle100\rangle_\alpha/\langle001\rangle_{Al_3Zr}$, $\langle112\rangle_\alpha/\langle481\rangle_{Al_3Zr}$ and $\langle112\rangle_\alpha/\langle221\rangle_{Al_3Zr}$. If a possible matching plane together with a possible matching crystal direction can form a group of OR, this matching crystal direction will be located in this matching plane. Therefore, the possible ORs between α phase and Al_3Zr can be predicted as follows: $\{111\}_\alpha//\{114\}_{Al_3Zr}$, $\langle110\rangle_\alpha//\langle401\rangle_{Al_3Zr}$; $\{111\}_\alpha//\{114\}_{Al_3Zr}$, $\langle110\rangle_\alpha//\langle110\rangle_{Al_3Zr}$; $\{200\}_\alpha//\{200\}_{Al_3Zr}$, $\langle110\rangle_\alpha//\langle401\rangle_{Al_3Zr}$; $\{200\}_\alpha//\{200\}_{Al_3Zr}$, $\langle100\rangle_\alpha//\langle100\rangle_{Al_3Zr}$; $\{220\}_\alpha//\{220\}_{Al_3Zr}$, $\langle100\rangle_\alpha//\langle001\rangle_{Al_3Zr}$; $\{220\}_\alpha//\{220\}_{Al_3Zr}$, $\langle110\rangle_\alpha//\langle110\rangle_{Al_3Zr}$; $\{220\}_\alpha//\{220\}_{Al_3Zr}$, $\langle112\rangle_\alpha//\langle221\rangle_{Al_3Zr}$; $\{220\}_\alpha//\{208\}_{Al_3Zr}$, $\langle100\rangle_\alpha//\langle100\rangle_{Al_3Zr}$; $\{220\}_\alpha//\{208\}_{Al_3Zr}$, $\langle110\rangle_\alpha//\langle401\rangle_{Al3Zr}$; $\{220\}_\alpha//\{208\}_{Al_3Zr}$, $\langle112\rangle_\alpha//\langle481\rangle_{Al_3Zr}$.

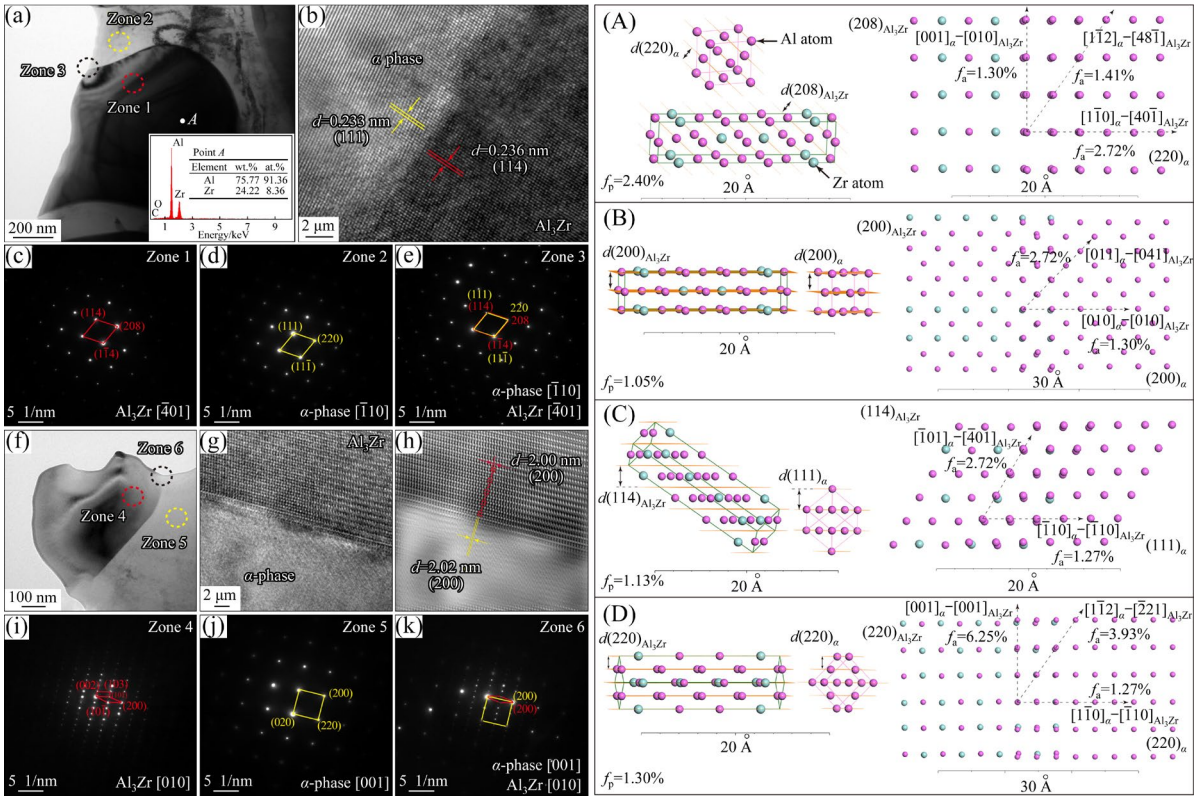

Fig. 15 (a, f) Al_3Zr particles in inoculated ZA22 alloy; (b, g) HRTEM images of interfacial microstructures shown in (a) and (f), respectively; (h) IFFT image of (g); (c−e) SAED patterns of Zones 1, 2 and 3 in (a), respectively; (i−k) SAED patterns of Zones 4, 5 and 6 in (f), respectively; (A−D) Lattice matching relationship between Al_3Zr and α phases

The observed results shown in Figs. 15(a−k) are included in the predicted results, and the crystallographic matching models corresponding to the observed results are shown in Figs. 15(A−D). It is worth noting that another possible OR is also predicted by the E2EM model, as shown in Fig. 15(D). This once again demonstrates the accuracy of the E2EM model.

Figure 16 shows the ORs between Al_2O_3 particles and α phase. It can be seen from the high-resolution images in Figs. 16(b−f) that nearly spherical Al_2O_3 particles have both coherent and non-coherent interfaces with α phase. Combined with the analysis results of FFT shown in Fig. 16(a′), it is confirmed that there is a coherent OR between Al_2O_3 particles and α phase: $(111)_\alpha // (11\bar{2}0)_{Al_2O_3}$. This OR can also be predicted by using the E2EM model: $(111)_\alpha // (11\bar{2}0)_{Al_2O_3}$, $[\bar{1}\,\bar{1}2]_\alpha // [\bar{1}101]_{Al_2O_3}$, and the crystal structures of α and Al_2O_3 phases and their lattice matching model are shown in Figs. 17(a) and (b), rerspectively. In addition, the presence of dislocations at locations near the interface between Al_2O_3 particles and α phase is found in Figs. 16(g) and (h), which further demonstrates the hindering effect of Al_2O_3 particles on dislocations on the soft α phase.

As mentioned above, a special Al_2O_3/Al_3Zr composite structure (Al_2O_3 wrapped with Al_3Zr) was found in both inoculant and inoculated ZA22 alloys. We assume that the Al_2O_3 particles with a higher melting point may have served as a nucleation substrate for the Al_3Zr particles with a relatively low melting point, resulting in the refinement of Al_3Zr phase. To confirm this conjecture, the OR between the two phases predicted using E2EM is provided in Fig. 18. It is found that the following ORs exist between the two phases: $(114)_{Al_3Zr} // (11\bar{2}0)_{Al_2O_3}$; $[\bar{8}41]_{Al_3Zr} // [\bar{1}101]_{Al_2O_3}$.

3.4 Effect of inoculation on tensile mechanical and damping properties of ZA22 alloy

Figure 19(a) shows the tensile stress−strain curves of the ZA22 alloys inoculated by different contents of (Al_2O_3+Al_3Zr)/Al composite inoculant. Combining the tensile strength and elongation in Figs. 19(b) and (c), it can be seen that the original

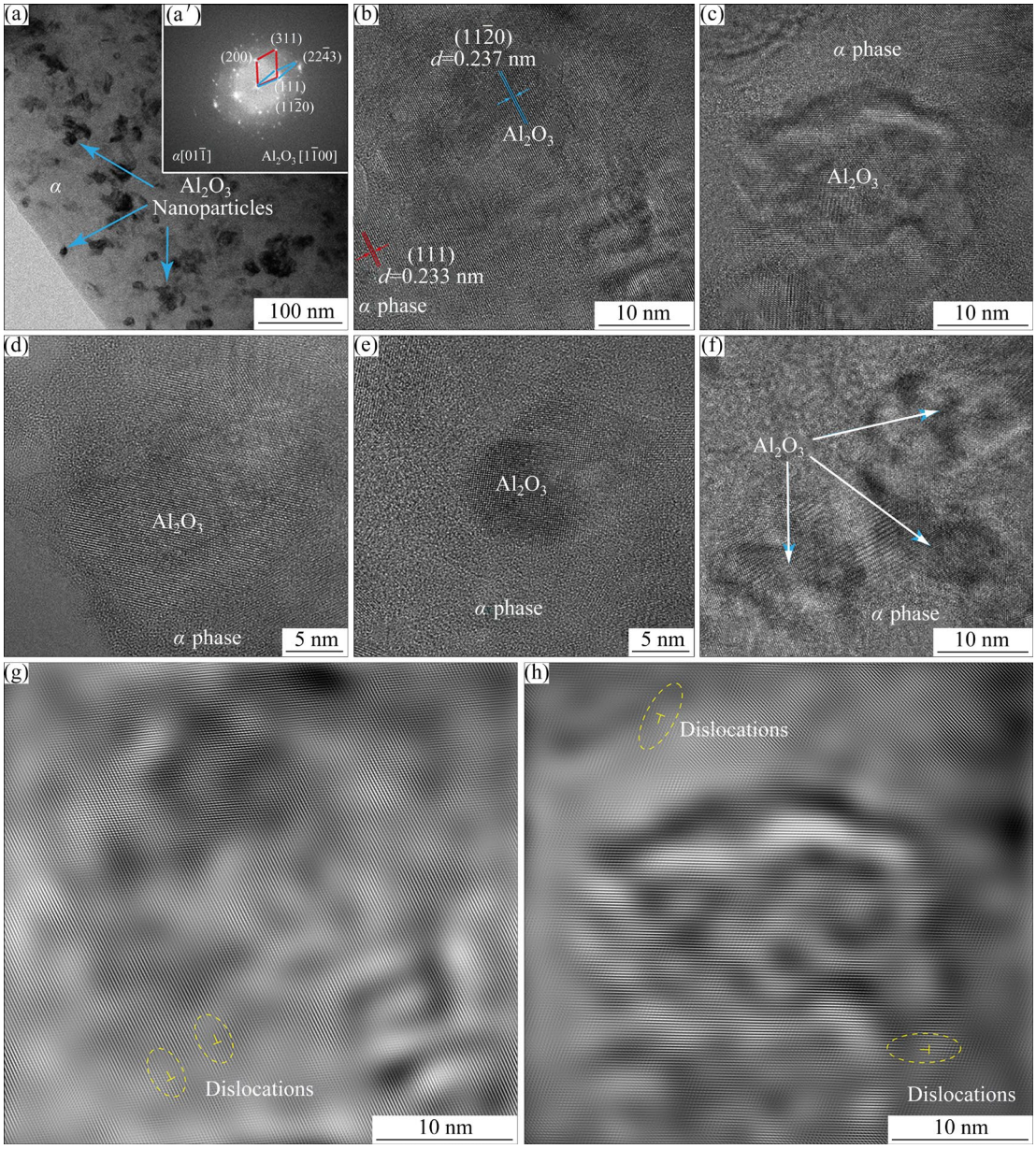

Fig. 16 (a) TEM image showing Al_2O_3 particles in α phase; (a′) FFT image of (b); (b−f) HRTEM images of Al_2O_3 particles at different positions in (a); (g, h) IFFT images from (b) and (c), respectively

ZA22 alloy has a tensile strength of 237 MPa and an elongation of 4.03%. With the increase of the content of inoculant, the tensile strength and elongation increase first and then decrease. When the content of inoculant is 1.0 wt.%, the tensile strength and elongation reach their highest values of 355 MPa and 7.62%, which are 49.79% and 89.08% higher than those of the original ZA22 alloy, respectively.

Figure 20(a) shows the damping property of different ZA22 alloys. It can be seen that with the increase of inoculant content, the damping (tan δ) of ZA22 alloy exhibits different changes in different temperature regions. For convenience, the damping−temperature curves are divided into three regions (Regions I, II and III): low temperature region (45−185 °C), medium temperature region (185−316 °C) and high temperature region (316−400 °C). In Region I, the damping of all the inoculated ZA22 alloys is lower than that of the original ZA22 alloy, but the gap between them decreases as the temperature rises. In Region II, the damping of the inoculated ZA22 alloy begins to be higher than that of the original ZA22 alloy, and the pattern is that the higher the inoculant content, the higher the starting temperature at which the former exceeds

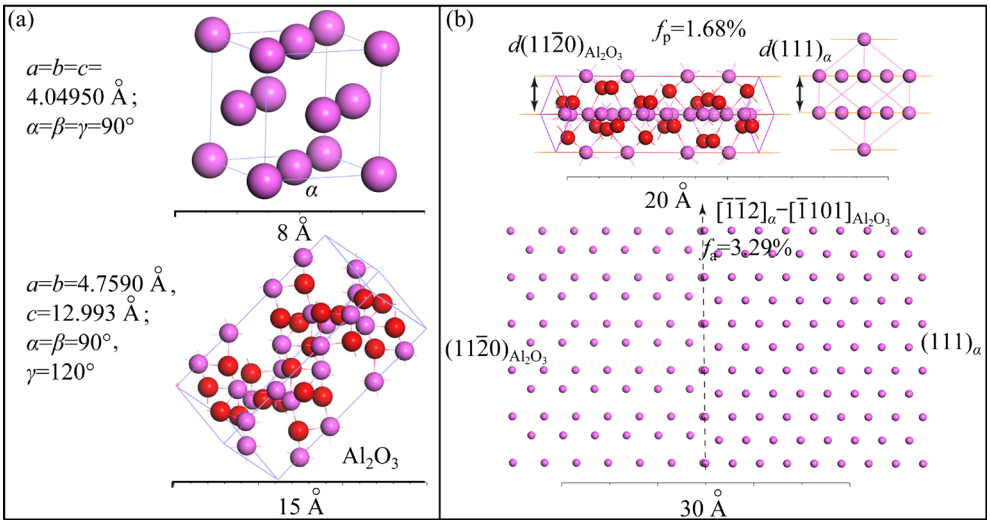

Fig. 17 Crystal structures of α and Al_2O_3 phases (a) and their lattice matching relationships (b)

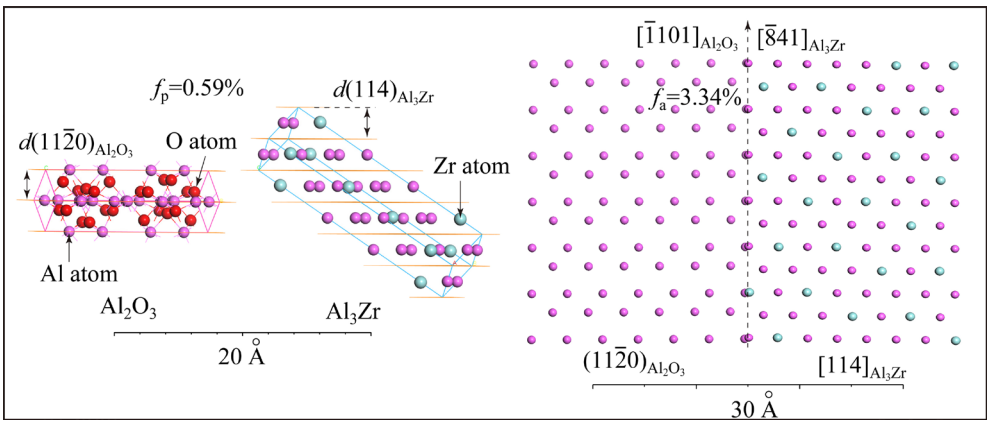

Fig. 18 Lattice matching relationship between Al_2O_3 and Al_3Zr phases

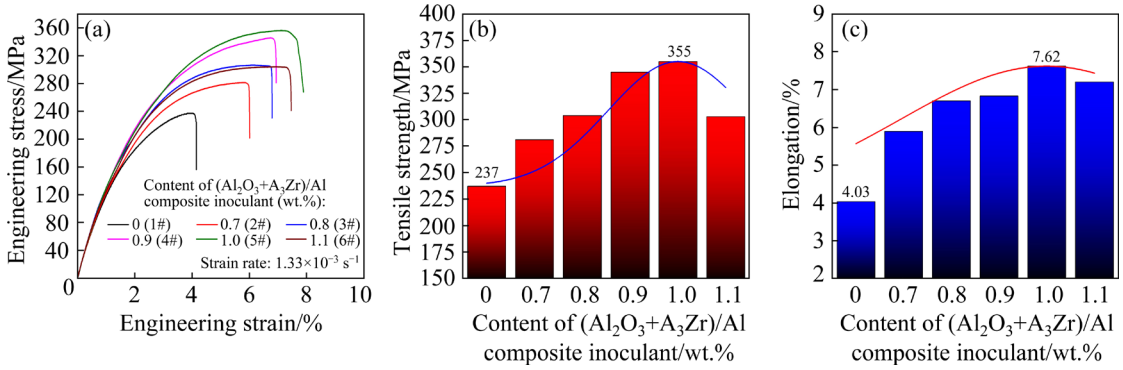

Fig. 19 Tensile stress−strain curves (a), tensile strength (b) and elongation (c) of ZA22 alloys

the latter. In Region III, the damping of all the inoculated ZA22 alloys is higher than that of the original ZA22 alloy, and the highest damping is obtained when the inoculant content reaches 1.0 wt.%. From Fig. 20(b), it can also be found that the damping peak resulting from the reverse eutectoid transformation increases and then decreases as the inoculant content increases. In addition, although the damping of the inoculated ZA22 alloys is lower than that of the original ZA22 alloy, the gap between them is actually not significant. It is worth noting that although the damping of ZA22 alloy slightly decreases at low temperatures after inoculation, it can still be maintained within the high damping range of 0.025−0.116. That is to say, inoculation can

significantly improve the mechanical properties of ZA22 alloy while maintaining the high damping property, which is extremely important for engineering applications.

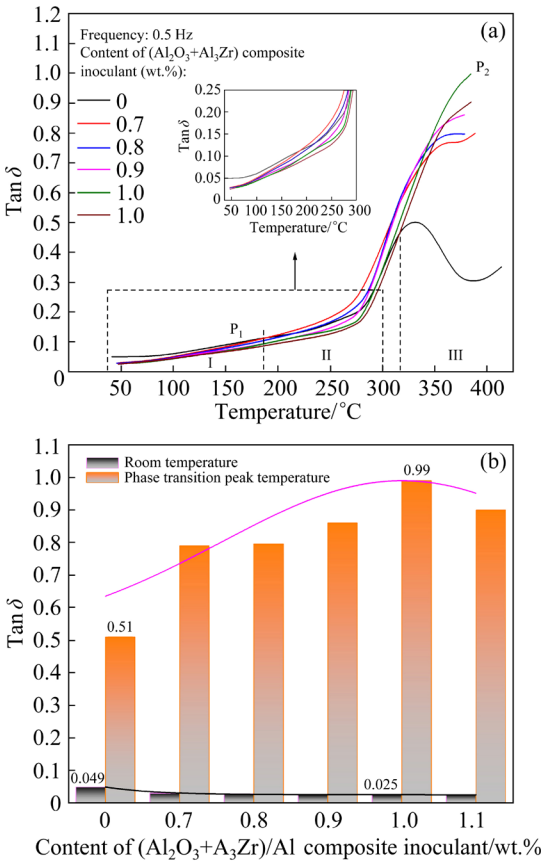

Fig. 20 Damping−temperature curves (a) and relationship between damping and (Al_2O_3+A_3Zr)/Al inoculant content (b) of ZA22 alloys at different temperatures

In this study, the α phase is significantly refined after inoculation, so fine grain strengthening is one of the main strengthening mechanisms of the inoculated ZA22 alloy. In addition, from Fig. 11 it is seen that the lamellar eutectoid structure is also refined after inoculation. Obviously, the finer the eutectoid structure, the greater the compressive stress between the lamellae [1,5,12], and the more difficult the sliding of interfaces, which also leads to the improvement of strength. From Figs. 11(h−k), it can also be seen that there is a coherent interface between the α phase and the η phase, and the two phases have the ORs of $(111)_\alpha//(10\bar{1}1)_\eta$ and $(200)_\alpha//(10\bar{1}1)_\eta$. The interplanar spacing mismatches between the two sets of crystal planes are different. The mismatch between $(111)_\alpha$ and $(10\bar{1}1)_\eta$ is 10.3%, and the mismatch between $(200)_\alpha$ and $(10\bar{1}1)_\eta$ is 3.3%. Obviously, lattice distortion is required between the crystal planes with a relatively large degree of mismatch to adjust their coherent interfaces (as shown in Fig. 11(i)). The stress field caused by the lattice distortion will hinder the motion of the dislocations and result in the improved strength of the ZA22 alloy. It has been reported that the coherent interface has superior load transfer efficiency, leading to higher strength of the material [31]. Therefore, in the present study, the coherent interface of the lamellar eutectoid structure also has a very important contribution to the improvement of strength of the inoculated ZA22 alloy. In addition, it is noteworthy that dislocations are formed near the coherent interface, as shown in Fig. 11(k), indicating that coherent interface with a small mismatch still has hindering effect on the slip of dislocations, which may also be the strengthening mechanism of coherent interface. Dispersion strengthening is another main strengthening mechanism, which is reflected in three aspects: (1) fine Al_2O_3 particles are uniformly distributed in the lamellar eutectoid structure, and they can pin the α/η interfaces and dislocations, leading to the improvement of strength; (2) nano-sized nearly spherical Al_2O_3 particles distributed inside α phase can improve the strength of the α phase by pinning dislocations; (3) Al_3Zr particles distributed at the α/η interfaces can hinder the sliding of interfaces, leading to the improvement of strength. In addition to the Orowan and Hall−Petch strengthening mechanisms shown in Fig. 21, there may also be strengthening effects of elastic mismatch and thermal mismatch caused by huge differences in the physical properties between Al_2O_3 and Al_3Zr particles and the matrix phase, which are collectively referred to as Taylor strengthening mechanism.

The improvement of elongation of the inoculated ZA22 alloy can be attributed to the aforementioned fine grain strengthening effect, as well as the shortening of the dendrite axis of α phase and the refinement of the spherical eutectic structure. When the α phase is dendritic in shape, there is severe stress concentration at the tips of its primary and secondary dendrite axes. Whereas when the α phase is nearly equiaxed in shape, the problem of stress concentration is largely alleviated, as indicated by the KAM maps shown in Figs. 7(d) and (h), thus improving the plasticity and toughness of the alloy. Another reason is the refinement of

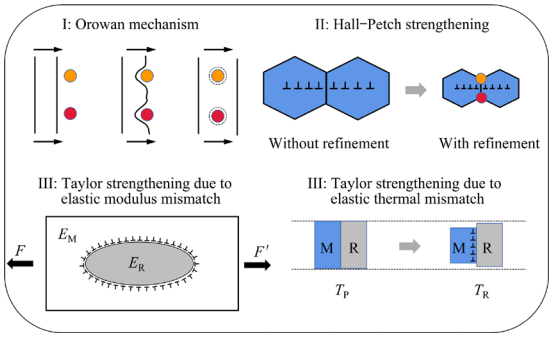

Fig. 21 Improving mechanisms of tensile mechanical properties of inoculated ZA22 alloys (E_M and E_R are the elastic moduli of the matrix and the reinforcement, respectively; T_P and T_R are the processing and room temperatures, respectively)

granular eutectic structure. As shown in Fig. 12, the granular eutectic structure is also refined after inoculation. It has been reported that when the size of α or η phase is less than 10 μm, ZA22 alloy will exhibit superplasticity [32,33]. Obviously, the refined eutectic structure shown in Fig. 12 can make a positive contribution to the improvement of plasticity of the ZA22 alloy. In addition, as mentioned above, the core−shell structure shown in Figs. 12(e) and (f) can prevent collision between hard phases from causing microcracks, so it also contributes to the improvement of plasticity. Of course, in the special $\alpha/\eta/\alpha$ structure found in Fig. 13, the thin layer of η phase acts as a lubricant that promotes the sliding of α/α interface, thus contributing positively to the plasticity. It has been reported that the coherent interface enhanced the deformation compatibility of the two phases, resulting in the improvement of toughness [31]. Based on this theory, in this study, the coherent interface consisting of the soft α phase and the hard η phase can also be compatible with each other during deformation, allowing the plasticity of the refined ZA22 alloy to be enhanced. So the fine lamellar eutectoid structure with coherent interface can simultaneously improve the strength and plasticity of the alloy.

The damping property of ZA22 alloy is determined by the density and mobility of various interfaces (including grain boundary and phase boundary) [4,5]. After inoculation, the density of interfaces of ZA22 alloy increases significantly, but the introduction of Al_2O_3 and Al_3Zr particles imposes a pinning effect on the mobility of the interfaces. This is because the competition of these two influencing factors makes the damping of ZA22 alloy different in different temperature regions. As the atomic mobility at interfaces in low temperature region is relatively low, the decrease of damping caused by the pinning effect of hard particles at interfaces is higher than the contribution of interface density to the damping. Therefore, the damping in low temperature region is slightly decreased. However, in high temperature region, the atoms at the interface gain sufficient energy, so the interface can overcome the pinning force and start sliding.

4 Conclusions

(1) In situ (Al_2O_3+Al_3Zr)/Al composite inoculant was successfully fabricated. It is composed of Al matrix, as well as Al_2O_3 and Al_3Zr particles with different particle sizes. The in situ composite inoculant has a significant refining effect on the α phase in the ZA22 alloy. When the content of inoculant reaches 1.0 wt.%, the best refining effect is achieved, and the α phase can be refined to 14 μm from the original 100 μm. As the content of inoculant increases, the α phase undergoes an evolution process from dendritic shape to petal shape, then to granular shape, and finally to petal shape again.

(2) Al_3Zr has four groups of crystal planes that match well with the α phase, while Al_2O_3 has only one group, so Al_3Zr has a more effective refining effect on the α phase. In addition to the nucleation and growth around heterogeneous particles located at the center, it is interesting that the α phase can also exhibit epitaxial growth along a certain crystal plane of some larger Al_2O_3 and Al_3Zr particles as well as Al_2O_3/Al_3Zr composite structure.

(3) After inoculation, the tensile mechanical properties of the ZA22 alloy are significantly improved. The tensile strength and elongation of the ZA22 alloy with the best refining effect reach 355 MPa and 7.62%, which are 49.79% and 89.08% higher than those of the original ZA22 alloy, respectively. The improvement in the tensile strength can be attributed to the strengthening mechanisms of Orowan, Hall−Petch and Taylor, as well as the strengthening effect of coherent α/η interface in lamellar eutectoid structure. The improvement in the plasticity can be attributed to

the formation of equiaxed grains of α and η phases, the refinement of the granular eutectic structure, the formation of special η@α core−shell eutectic structure and layered $\alpha/\eta/\alpha$ structure, as well as the compatible deformation of coherent α/η interface in lamellar eutectoid structure. The damping of the inoculated ZA22 alloys slightly decreases at low temperatures, but significantly increases at high temperatures. The change in damping is a result of comprehensive effects of density and mobility changes of interfaces in the inoculated ZA22 alloys.

CRediT authorship contribution statement

Jian-jun ZHANG: Investigation, Data curation, Writing − Original draft; **Dong-mei LU:** Investigation, Methodology; **Fu-xing YIN:** Conceptualization; **Hui YU:** Investigation, Conceptualization; **Pu-guang JI:** Funding acquisition; **Yu-fang LI:** Investigation; **Qing-zhou WANG:** Conceptualization, Project administration, Funding acquisition.

Declaration of competing interest

The authors declare that they have no known competing financial interests or personal relationships that could have appeared to influence the work reported in this paper.

Acknowledgments

This work was supported by the Foundation Strengthening Program of China (No. 2019-JCJQ-ZD-142-00), the Natural Science Foundation of Hebei Province, China (No. E2021202017), and the Foundation of Guangdong Academy of Sciences, China (No. 2021GDASYL- 20210102002).

References

[1] LIU Ya-fei, YIN Fu-xing, YU Hui, FENG Jian-hang, JI Pu-guang, ZHANG Jian-jun, JIAO Zhi-xian, LIU Li, WANG Qing-zhou. Microstructural evolution, damping and tensile mechanical properties of multilayer Zn−22Al alloy fabricated by accumulative roll bonding (ARB) [J]. Materials Science and Engineering A, 2022, 840: 142911.

[2] GIRISH B M, PRAKASH K R, SATISH B M, JAIN P K, PRABHAKAR P. An investigation into the effects of graphite particles on the damping behavior of ZA-27 alloy composite material [J]. Materials & Design, 2011, 32: 1050−1056.

[3] YOUSEFI D, TAGHIABADI R, SHAERI M H. Effect of multi-pass multi-directional forging on tribological properties of Si-rich eutectoid ZA alloys [J]. Transactions of Nonferrous Metals Society of China, 2021, 31: 2024−2038.

[4] ZHANG Jian-jun, WANG Qing-zhou, JIAO Zhi-xian, YIN Fu-xing, CUI Chun-xiang, YAO Chang. Effects of combined use of inoculation and modification heat treatment on microstructure, damping and mechanical properties of Zn−Al eutectoid alloy [J]. Materials Science and Engineering A, 2020, 790: 139740.

[5] LI Nan, LIU Xiao-jin, WANG Qing-zhou, CUI Chun-xiang, YIN Fu-xing, JI Xiang-wei. Effect of combined addition of Al−Ti−B ribbon and Zr element on the microstructure, mechanical and damping properties of ZA22 alloy [J]. Materials & Design, 2017, 127: 97−105.

[6] DEMIRTAS M, ATLI K C, YANAR H, PURCEK G. Effect of grain refinement and phase composition on room temperature superplasticity and damping capacity of dual-phase Zn−Al alloys [J]. Journal of Materials Research, 2018, 33: 1032−1045.

[7] NAIK G M, SACHIN B, BADIGER R I, HEBBALE A M. Microstructure and mechanical properties of TiO_2 reinforced ZA22 metal matrix composite [J]. Materials Today Proceedings, 2021, 35: 303−307.

[8] YU S, LI W, HE Z. Study on tensile strengths of Al_2O_3 short fiber reinforced Zn−Al alloy composites at elevated temperatures [J]. Journal of Alloys and Compounds, 2007, 431: L8−L11.

[9] AL-QAWABAH S M A, ZAID A I O. Effect of Mo addition to ZA22 alloy grain refined by Ti−B on its metallurgical and mechanical characteristics in the as cast condition [J]. Materials Science Forum, 2017, 886: 64−68.

[10] YOUSEFI D, TAGHIABADI R, SHAERI M H, ABEDINZADEH P. Enhancing the mechanical properties of Si particle reinforced ZA22 composite by Ti−B modification [J]. International Journal of Metalcasting, 2021, 15: 206−215.

[11] SKENAZI A F, PELERIN J, COUTSOURADIS D, MAGNUS B, MEEUS M. Some recent developments in the improvement of the mechanical properties of zinc foundry alloys [J]. Metall, 1983, 37: 898−902.

[12] ZHANG Jian-jun, YIN Fu-xing, JIANG Bi-nan, WANG Qing-zhou, YU Hui, JIAO Zhi-xian, LIU Li, JI Pu-guang, LIU Ya-fei. A novel in situ (Al_3Ni+Al_3Ti)/Al composite inoculant and its effects on the microstructure, damping and mechanical properties of Zn−Al eutectoid alloy [J]. Metallurgical and Materials Transactions A, 2022, 53: 2099−2115.

[13] MAURYA P, KOTA N, GIBMEIER J, WANNER A, ROY S. Review on study of internal load transfer in metal matrix composites using diffraction techniques [J]. Materials Science and Engineering A, 2022, 840: 142973.

[14] BALOG M, KRIZIK P, DVORAK J, BAJANA O, KRAJCOVIC J, DRIENOVSKY M. Industrially fabricated in-situ Al-AlN metal matrix composites (Part B): The mechanical, creep, and thermal properties [J]. Journal of Alloys and Compounds, 2022, 909: 164720.

[15] JARZĄBEK D M, CHMIELEWSKI M, WOJCIE-CHOWSKI T. The measurement of the adhesion force between ceramic particles and metal matrix in ceramic reinforced-metal matrix composites [J]. Composites (Part A): Applied Science and Manufacturing, 2015, 76: 124−130.

[16] GILL R S, SAMRA, P S, KUMAR A. Effect of different types of reinforcement on tribological properties of aluminium metal matrix composites (MMCs)—A review of recent studies [J]. Materials Today: Proceedings, 2022, 56: 3094−3101.

[17] RAMNATH B V, ELANCHEZHIAN C, ANNAMALAI R M, ARAVIND S, ATREYA T S A, VIGNESH V, SUBRAMANIAN C. Aluminium metal matrix composites—A review [J]. Reviews on Advanced Materials Science, 2014, 38: 55−60.

[18] HODDER K J, IZADI H, MCDONALD A G, GERLICH A P. Fabrication of aluminum−alumina metal matrix composites via cold gas dynamic spraying at low pressure followed by friction stir processing [J]. Materials Science and Engineering A, 2012, 556: 114−121.
[19] BHOI N K, SINGH H, PRATAP S. Developments in the aluminum metal matrix composites reinforced by micro/nano particles—A review [J]. Journal of Composite Materials, 2020, 54: 813−833.
[20] XU Jia-sheng, CHEN Gang, ZHANG Zhen-ya, ZHAO Yu-tao, ZHANG Ting, ZHANG Chen-ting-ying, DING Da-li. Effect of Al−3wt.%Al_2O_3 master alloy fabricated by calcined kaolin on grain refinement and mechanical properties of A356 alloy [J]. Journal of Alloys and Compounds, 2021, 862: 158512.
[21] XU Tuo, LI Gui-rong, XIE Meng-lei, LIU Ming, ZHANG De, ZHAO Yu-tao, CHEN Gang, KAI Xi-zhou. Microstructure and mechanical properties of in-situ nano γ-Al_2O_{3p}/A356 aluminum matrix composite [J]. Journal of Alloys and Compounds, 2019, 787: 72−85.
[22] EDWARDS T E J, XIE T L, DELLA VENTURA N M, CASARI D, GUERRA C, HUSZÁR E, MAEDER X, SCHWIEDRZIK J J, UTKE I, PETHÖ L, MICHLER J. On the thinnest Al_2O_3 interlayers in Al-based nanolaminates to enhance strength, and the role of constraint [J]. Acta Materialia, 2022, 240: 118345.
[23] ZHAO Y T, ZHANG S L, CHEN G, CHENG X N, WANG C Q. In situ $(Al_2O_3+Al_3Zr)_{np}$/Al nanocomposites synthesized by magneto-chemical melt reaction [J]. Composites Science and Technology, 2008, 68: 1463−1470.
[24] LI G R, ZHAO Y T, WANG H M, CHEN G, DAI Q X, CHENG X N. Fabrication and properties of *in situ* $(Al_3Zr+Al_2O_3)_p$/A356 composites cast by permanent mould and squeeze casting [J]. Journal of Alloys and Compounds, 2009, 471: 530−535.
[25] ZHU H G, MIN J, LI J L, AI Y L, GE L Q, WANG H Z. In situ fabrication of (α-Al_2O_3+Al_3Zr)/Al composites in an Al−ZrO_2 system [J]. Composites Science and Technology, 2010, 70: 2183−2189.
[26] WANG Tao, JIN Zhan-peng, ZHAO Ji-cheng. Thermodynamic assessment of the Al−Zr binary system [J]. Journal of Phase Equilibria and Diffusion, 2001, 22: 544−551.
[27] SONG Zi-zheng, NIU Ran-ming, CUI Xiang-yuan, BOBRUK E V, MURASHKIN M Y, ENIKEEV N A, GU Ji, SONG Min, BHATIA V, RINGER S P, VALIEV R Z, LIAO Xiao-zhou. Mechanism of room-temperature superplasticity in ultrafine-grained Al−Zn alloys [J]. Acta Materialia, 2023, 246: 118671.
[28] STRAUMAL B B, SAUVAGE X, BARETZKY B, MAZILKIN A A, VALIEV R Z. Grain boundary films in Al−Zn alloys after high pressure torsion [J]. Scripta Materialia, 2014, 70: 59−62.
[29] ZHANG M X, KELLY P M, EASTON M A, TAYLOR J A. Crystallographic study of grain refinement in aluminum alloys using the edge-to-edge matching model [J]. Acta Materialia, 2005, 53: 1427−1438.
[30] JING Li-jun, PAN Ye, LU Tao, PI Jin-hong, GU Teng-fei. Nucleation potency prediction of LaB_6 with E2EM model and its influence on microstructure and tensile properties of Al−7Si−0.3Mg alloy [J]. Transactions of Nonferrous Metals Society of China, 2018, 28: 1687−1694.
[31] MA Li-shi, ZHANG Xiang, DUAN Yong-hua, GUO Si-yuan, ZHAO Dong-dong, HE Chun-nian, ZHAO Nai-qin. Constructing the coherent transition interface structure for enhancing strength and ductility of hexagonal boron nitride nanosheets/Al composites [J]. Journal of Materials Science & Technology, 2023, 145: 235−248.
[32] KAWASAKI M, LANGDON T G. The significance of grain boundary sliding in the superplastic Zn−22%Al alloy processed by ECAP [J]. Journal of Materials Science, 2013, 48: 4730−4741.
[33] LANGDON T G. Seventy-five years of superplasticity: historic developments and new opportunities [J]. Journal of Materials Science, 2009, 44: 5998−6010.

原位生成 Al_2O_3 和 Al_3Zr 颗粒强化高阻尼 Zn−Al 共析合金的显微组织和力学性能

张建军[1]，陆东梅[2]，殷福星[3]，余 晖[1]，冀璞光[1]，李玉芳[1]，王清周[1]

1. 河北工业大学 材料科学与工程学院 高性能轧辊材料与复合成形全国重点实验室，天津 300130；
2. 河北工业大学 理学院，天津 300130；
3. 广东省科学院 新材料研究所，广州 510651

摘 要：Zn−Al 共析合金(ZA22)具有超高的阻尼性能，但是其力学性能仍相对较低。为了同时提高 ZA22 合金的抗拉强度和塑性，设计并使用了一种含有原位生成的 Al_2O_3 和 Al_3Zr 颗粒的新型 Al 基复合孕育剂来强化 ZA22 合金。 ZA22 合金的显微组织被显著细化，细小的 Al_2O_3 颗粒均匀分布在 α 相和片状共析组织中，而 Al_3Zr 颗粒则分布在 α 相和 α/η 的界面处。性能测试结果表明，孕育细化 ZA22 合金的拉伸力学性能得到了显著提高。最大抗拉强度和伸长率分别达到 355 MPa 和 7.62%，分别为原始 ZA22 合金的 1.50 倍和 1.89 倍。力学性能的提高可归因于细化显微组织中构建的多重强化和增韧因子。

关键词：ZA22 合金；Al_2O_3；Al_3Zr；显微组织细化；抗拉强度；伸长率

(Edited by Wei-ping CHEN)